Research Article | Vol. 13, No. 2 / 1 Feb 2022 / Biomedical Optics Express 850

Biomedical Optics EXPRESS

Development and ex-vivo validation of 36G polyimide cannulas integrating a guiding miniaturized OCT probe for robotic assisted subretinal injections

ALEXANDRE ABID,[1,2] RENAUD DUVAL,[3,4] AND CHRISTOS BOUTOPOULOS[1,2,4,*]

[1] *Institute of Biomedical Engineering, University of Montreal, Montreal, Quebec, Canada*
[2] *Maisonneuve-Rosemont Hospital Research Centre, Montreal, Quebec, Canada*
[3] *Maisonneuve-Rosemont Hospital, Montreal, Quebec, Canada*
[4] *Department of Ophthalmology, University of Montreal, Montreal, Quebec, Canada*
[*] *christos.boutopoulos@umontreal.ca*

Abstract: We introduced and validated a method to encase guiding optical coherence tomography (OCT) probes into clinically relevant 36G polyimide subretinal injection (SI) cannulas. Modified SI cannulas presented consistent flow capacity and tolerated the typical mechanical stress encountered in clinical use without significant loss of sensitivity. We also developed an approach that uses a micromanipulator, modified SI cannulas, and an intuitive graphical user interface to enable precise SI. We tested the system using ex-vivo porcine eyes and we found a high SI success ratio 95.0% (95% CI: 83.1–99.4). We also found that 75% of the injected volume ends up at the subretinal space. Finally, we showed that this approach can be applied to transform commercial 40G SI cannulas to guided cannulas. The modified cannulas and guiding approach can enable precise and reproducible SI of novel gene and cell therapies targeting retinal diseases.

1. Introduction

Subretinal injection (SI) of drugs is a challenging surgical intervention aiming to restore and/or preserve the vision of patients suffering from retinal diseases. To perform SI, a cannula is inserted under the retina, a delicate tissue layer (0.10–0.35 mm) that lines the inside of the eye. The SI drug delivery route is more efficient compared to intravitreal injection as it enables a more direct effect for therapies targeting the retina. Furthermore the subretinal space is anatomically closed with better immune privilege compared to the vitreous cavity [1]. Thus, SI is the most common route for ophthalmic gene and cell therapy. In 2017, the SI route was used in 67% of gene therapy clinal trials [2].

Nevertheless, the SI route remains at the edge of human physiological capacity. Physiological hand tremor and micro jerks are on the order of 200 µm (i.e., comparable to the retinal layer thickness) in static position [3]. Surgeons monitor the spatial distribution of a subretinal bleb with the help of an operating microscope to access the success of a SI. However, this is quite a subjective criterion, imposing uncertainty for the effectively delivered dose. Even though this problematic is recognized [4], studies focusing on its impact on the therapeutic outcome are yet to be performed. For non-optimal SI, reflux of the drug in the vitreous may occur [4]. Poorly executed SI can also induce damage to the retina, such as retinal detachment, vitreous hemorrhage, recurrence of submacular hemorrhage, and postoperative development of choroidal neovascularization [1]. The SI outcome is sensitive to individuals' surgical skills and learning curve [5]. The size of the cannulas used in SI plays an important role in the procedure. Throughout the years, SI are getting smaller in diameter (down to 41G) to reduce potential damage to the retina [6].

#448471 https://doi.org/10.1364/BOE.448471
Journal © 2022 Received 18 Nov 2021; revised 12 Jan 2022; accepted 13 Jan 2022; published 20 Jan 2022

Biomedical Optics EXPRESS

Various approaches have been proposed to improve the efficacy of SI. Robot-assisted SI injections were demonstrated in-vitro [7], with in-vivo work in rabbits [8], and clinically [9]. Those robot-assisted technologies enhance precision by removing surgeons' hand-tremor and can be combined with approaches that exploit monocular vision for guidance [10]. However, surgeons continue to rely on subjective evaluation to advance the cannula towards the targeted injection depth. An approach that uses semi-automated magnetic-based navigation was tested for guided SI in ex-vivo porcine eyes [11]. A translation limitation of this technology is the fact that it uses a bulky guiding magnetic system.

Optical coherence tomography (OCT) systems employ a technique known as low-coherence interferometry to generate tomographic images of tissue. OCT is a non-invasive technique of relatively short imaging penetration depth (a few mm) but achieves high image resolution (1–15 μm) [12,13]. Recently, state-of-the art systems have enabled intraoperative OCT (iOCT) imaging via integration with surgical microscopes [14]. iOCT is used as complementary imaging modality for intraocular maneuvers [14]. However, iOCT systems are designed to guide surgeons and not to execute a maneuver requiring high precision. Thus, the SI efficacy depends on their ability to interpret real-time OCT imaging and to assess/control the SI cannula insertion depth accordingly. Presently, the availability of this technology is limited because it requires high-end equipment that has yet to become standard for operating theaters [15].

Fiber-based endoscopic OCT probes have been used as alternative visualization tools for eye surgery [16,17]. OCT-guided SI were demonstrated with the use of a handheld tool [18]. In this work, the cannula design comprised of a fiber probe attached to a 34G needle. The handheld tool compensated for hand tremors and employed distal sensing to control SI in dissected ex-vivo porcine retina. A variation of this approach uses a second fiber attached to the needle to estimate the injection angle [19]. The latter can improve the injection precision for systems that use the retinal front as reference point when setting the injection depth. Those approaches are limited by the fact that external fiber attachment increases the thickens of the SI assembly. Although applicability to clinically relevant SI cannulas should be in principle feasible, it has yet to be demonstrated.

Previous approaches to increase SI injection efficacy focus on removing surgeon's hand tremor and/or on providing real-time imaging data, which can help them assess/control the insertion of the SI cannula towards the RPE. Yet, SI efficacy can be enhanced by assigning this fine step to a robot that "knows" the distance between the cannula and the Retinal Pigment Epithelium (RPE) with micrometric precision. The encasement of OCT probes into clinically used and/or clinically relevant SI cannulas would represent an important advancement towards the development and clinical adoption of such systems.

In this work, we sought to address this challenge. We present an approach to encase miniaturized OCT probes into clinically relevant polyimide 36G SI cannulas. We validated the flow capacity and mechanical robustness of the developed cannulas as well as the sensitivity of the encased probes. We used a semi-automated system with a user-friendly interface to perform robotic controlled SI in ex-vivo porcine eyes. We validated the SI success rate as well as the model drug reflux using external OCT imaging. Finally, we show that our approach can be applied to commercially available metallic 40G SI cannulas.

2. Materials and methods

2.1. Probe fabrication

We used commercially available 125 μm - thick fibers (Single Mode (SM): SM800-5.6-125, Graded-Index (GRIN): GIF625, Coreless (CL): FG 125LA, Thorlabs, USA) and telecom splicing/cleaving equipment (AI-6, Signal Fire, China) for the fabrication of the OCT probes. The commercially available fiber components are thicker than the inner diameter (~ 120 μm) of 36G cannulas. To fabricate miniaturized fiber probes, we used a previously reported approach

Biomedical Optics EXPRESS

that allows miniaturization of GRIN-based probes down to 70 µm using chemical etching [20]. To maximize the sensitivity in detecting the retina, we sought for a probe that focuses the exiting beam at a 200 µm distance from its distal tip once immersed in the vitreous. We used a theoretical model [20] to design such probes and opted for a 320 µm GRIN fiber component spliced directly to the SM fiber. Finally, a protective CL fiber was spliced to the assembly and cleaved to a length of 50 µm. We miniaturized the probe down to 70 µm in thickness by immersing it in hydrofluoric acid for 20 minutes.

2.2. Assembling of OCT cannulas

We used two types of SI cannulas: 1) a home-made 36G polyimide cannula (Fig. 1 and 2) a commercial 40G metallic cannula (#3261, MedOne Surgical, Inc., USA) (Fig. 8). To assemble the home-made SI cannula, we first inserted a 60-mm long 36G polyimide tube (95820-00, Cole-Parmer, USA) into a 25G blunt needle. We arranged the assembly in such a way that the front end of the polyimide tube would extend 2 mm from the needle shaft, whereas its back end would remain accessible from the needle hub. Once the desired alignment was achieved, we used a medical device adhesive product (AA3926-high, Loctite, USA) to glue the two parts of the assembly. A schematic representation of the assembling steps can be found in Fig. S1(a). This architecture is widely used in commercial polyimide-based SI cannulas. Yet, in commercial products the back end of the polyimide tube is not accessible, thus impossible to insert the probe from the needle hub. In our home-made version, we inserted the miniaturized OCT probes through the needle hub up to the polyimide tube front end. Then, we fixed the fiber at a 4-way stopcock (UZ-30600-12, Cole-Parmer) using silicone glue, which also sealed the port (Fig. 1(a)). For modifying commercial 40G SI metallic cannulas, we first cut their beveled tip. Then, we inserted the miniaturized OCT probe through the needle hub and fixed it at the 4-way stopcock. Note that contrary to polyimide-based SI cannulas, the design of the commercial metallic cannula permits insertion of the probe via the needle hub (Fig. S1(b)).

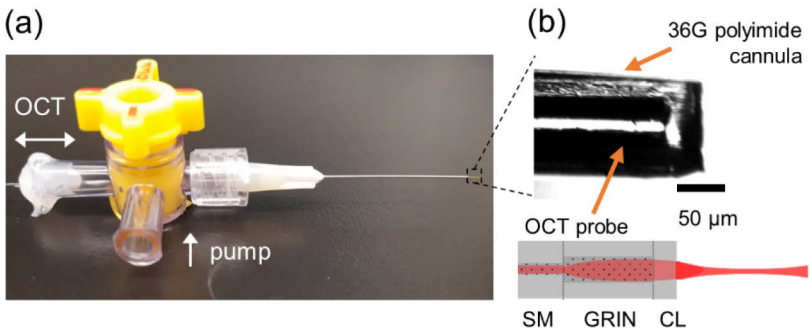

Fig. 1. a) A SI cannula assembly composed of a four-way stopcock, a 25G needle, a 36G polyimide cannula, and an encased OCT probe. b) Closeup picture of the polyimide cannula tip and encased probe. The schematic at the bottom shows the fiber components of the probe, i.e., SM: Single Mode fiber, GRIN: Graded-index fiber, CL: Coreless fiber. The dotted dark gray areas represent the fibers' core, whereas the light gray areas represent the fiber's cladding.

2.3. OCT and injection systems

Figure 2(a) presents an overview of the system that we used for OCT-controlled SI. We mounded modified home-made 36G SI cannulas or commercial 40G SI cannulas to a motorized micromanipulator (QUAD, Sutter instrument, USA) using a 4-way stopcock. The latter facilitated connection to a microinjection pump (PLI-100 Pico-Injector, Harvard Apparatus, USA) and to the

Biomedical Optics EXPRESS

OCT system (Fig. 2(b) and 2(c)). We used a homemade spectral-domain OCT (SD-OCT) system, composed of an infrared laser (central wavelength: 840 nm bandwidth: 50 nm, SLD-37-HP, Superlum, Ireland), an optical isolator (850 nm multimode isolator, AC Photonics Inc., USA), a 50:50 fiber coupler (AC Photonics Inc., USA), a variable optical attenuator (VOA) (V800A, Thorlabs, USA), and a compact spectrometer (USB 4000, Ocean Optics, USA). The laser power at the probe exit was ~ 0.3 mW. We used a LabVIEW based program to apply spectrometer k-space calibration, background subtraction, signal averaging as well as a digital-to-analog converter (DAC) (Labjack U3, Labjack, USA) to control the pump and VOA.

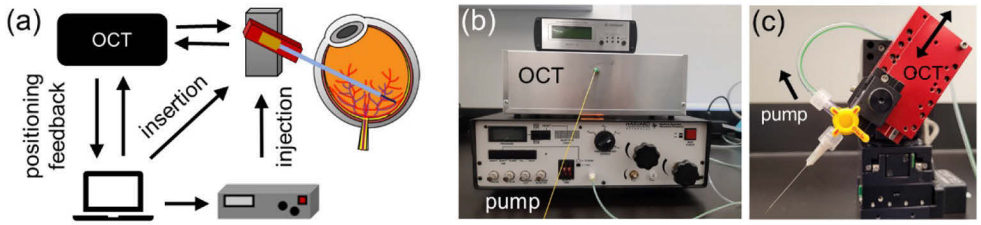

Fig. 2. a) Schematic overview of OCT-controlled SI system. b) Picture of the home-made OCT and injection pump. c) Picture of the 4-axis micromanipulator with an attached modified 36 SI cannula. The arrows indicate the connection to the pump and OCT.

2.4. Control algorithm and user interface

We developed a guiding algorithm and graphical user interface (GUI) using LabVIEW. First, we converted the spectrogram to A-scans using a fast Fourier transform (FFT). To perform background subtraction, we inserted modified cannulas into the eyeball and registered a reference signal, which we then subtracted from subsequent A-scan readings. This approach suppressed the DC component of the signal and other system artifacts. We performed real-time averaging of 10 A-scans to increase the signal over noise ratio (SNR). We displaced the modified cannulas towards the retina either manually using the micromanipulator control knob or automatically. For the automatic approaching, users defined a target value for the modified cannula-retina distance (from 150 to 500 μm). They also defined an SNR threshold (from 15 to 45 dB) for associating the OCT signal to the front layer of the retina. The threshold was set after assessing test M-scans, whereas its range reflects the effect of the approaching angle and eye condition on the SNR. In the automatic approach, the micromanipulator displaced the modified SI towards the retina until the SNR threshold was reached at a predetermined distance. Once the approach was completed, an M-scan of the retina was depicted on the LabVIEW GUI. Using M-scans, the users were able to identify the front and back part of the retina, i.e., the outer layer of the Inner Limiting Membrane (ILM) and the RPE. The M-scan of an ex-vivo pig retina can be appreciated in Fig. 5(b), where both the ILM and RPE are clearly defined. The users selected the desired injection volume and initiated automatic injections at the desired depth by clicking directly on the M-scan.

2.5. Calculation of subretinal bleb volume from volumetric OCT scans

We used external OCT visualization to quantify the volume of subretinal blebs. We acquired volumetric scans of the retinal before and after SI using an OQ Labscope 2.0 (Lumedica, USA) We automatically detected the front surface of the retina in those volumetric scans by processing each B-scan before and after the SI, using a home-made segmentation algorithm developed in MATLAB. The segmentation algorithm uses binarization and image processing. An indicative result of this process is shown in Fig. 7(c) and 7(d), where the front surface of the retina is traced with red before injection and blue after injection. We considered the measured retinal

Biomedical Optics EXPRESS

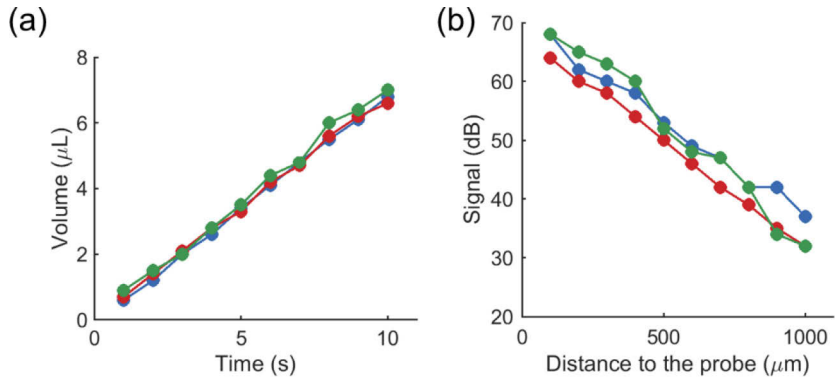

Fig. 3. a) Inter-cannula (n = 3) flow calibration measurements at 5 psi injection pressure. b) Inter-cannula (n = 3) OCT signal roll-off.

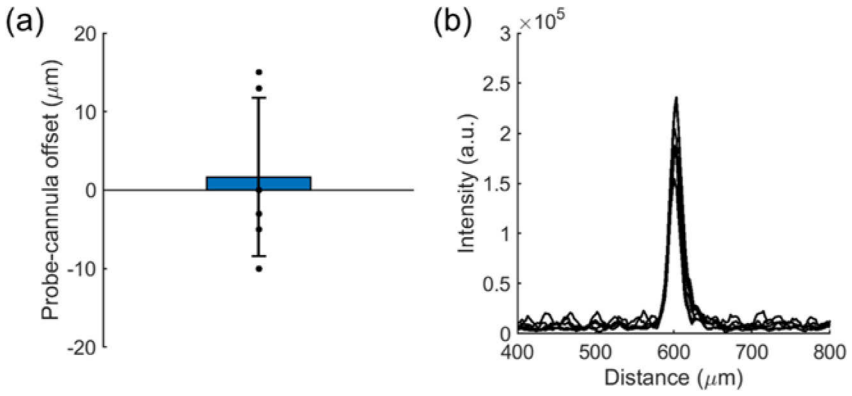

Fig. 4. a) Positioning offset between the cannula tip and the probe tip for six independent bending tests performed on the same probe. The error bar represents standard deviation. b) A-scans of an aluminum mirror performed with a SI cannula exposed to bending stress. Each A-scan was acquired after an independent bending experiment (n = 6).

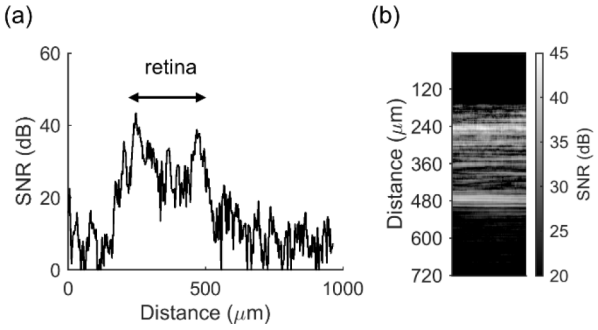

Fig. 5. Representative OCT signals acquired from porcine retina ex-vivo: a) A-scan and b) M-san. Those signals were displayed via a GUI interface (see Visualization 2, Visualization 3), allowing the user to identify the front and back part of the retina and to select a cannula insertion target via clicking on the M-scan.

Biomedical Optics EXPRESS

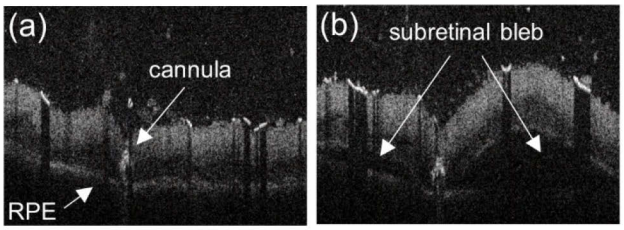

Fig. 6. Validation of an OCT-controlled automatic SI using external OCT visualization (B-scans) of the injection process. a) The SI cannula can be identified inside the retina after the automatic penetration. b) Subretinal bleb formation indicating a successful SI.

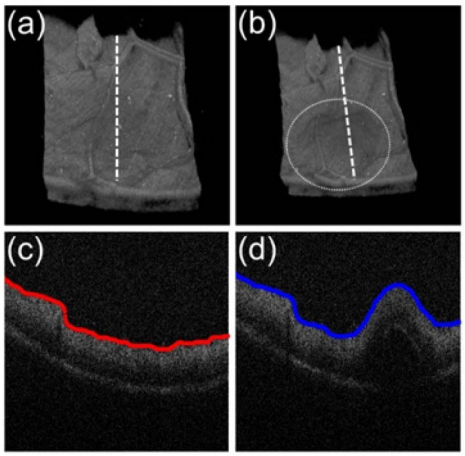

Fig. 7. (a-b) Indicative volumetric OCT scans of an ex-vivo pig retina (a) before and (b) after a SI. The white doted circle indicates the formed bleb, whereas the dashed line indicates the plane used to extract a representative B-scan. (c-d) Indicative B-scans (c) before and (d) after a SI. The red line shows the segmented front part of the retina before the injection, whereas the blue line shows the same after the injection.

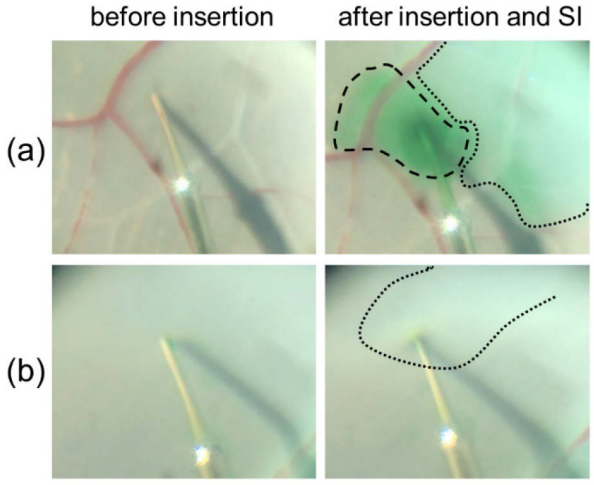

Fig. 8. Microscope pictures taken before and after performing OCT controlled SI in an ex-vivo porcine eye with a modified 40G cannula. a) Shallow SI cannula penetration resulted in liquid reflux b) No reflux was observed when the RPE was targeted. Black dotted lines indicate subretinal bleb formation, whereas the dashed line indicates reflux.

Biomedical Optics EXPRESS

displacement along entire B-scans (i.e., the area contained between the green and red lines) and the B-scan spacing to derive the subretinal bleb volume.

3. Results

3.1. Flow capacity and optical properties of modified 36G SI cannulas

A modified cannula has a reduced lumen cross section, thus compromised flow rate compared to a non-modified cannula. Here, we sought to validate whether modified cannulas maintain sufficient flow capacity for a clinically relevant injection pressure of 5 psi. We found that the average flow rate was (0.68 ± 0.02 µL/s). We also found only marginal variability of the flow rate among different probes (Fig. 3). The volumetric flow rate for modified cannulas can be calculated using the Poiseuille equation for an annular section [Eq. (1)]:

$$Q = \frac{\Delta p \cdot \pi}{8 \cdot \mu \cdot L}\left(R_2{}^4 - R_1{}^4 - \frac{\left(R_2{}^2 - R_1{}^2\right)^2}{\ln\left(\frac{R_2}{R_1}\right)}\right) \tag{1}$$

Where Δp is the pressure difference between the two ends of the cannula, L is the length of the cannula, μ is the dynamic viscosity, R_2 is the outer radius of the annulus, and R_1 is the inner radius of the annulus. Considering that the OCT probe diameter is 70 µm, one might calculate the volumetric flow rate for a modified 36G SI cannula (125 µm inner diameter) to 9% of that of an unmodified 36 SI cannula. This corresponds to the volumetric flow rate of an unmodified 48G SI cannula.

Next, we sought to validate whether the OCT probes maintain their optical properties once inserted into the cannula. Using a previously reported approach [20], we acquired SNR measurements be varying the distance between modified cannulas and a microscope slide. We found that the encased probes present similar peak SNR and sensitivity roll-off compared to that reported for non-encased counterpart probes [20].

Taken together, these results indicate that modified cannulas present sufficient flow capacity and that encased probes maintain their optical properties. Moreover, the consistency in both flow capacity and SNR measurements demonstrates that the fabrication process is reliable.

3.2. Bending stress tolerance of modified 36G SI cannulas

In a clinical practice, SI injection cannulas can subject to mechanical stress. For example, the polyimide cannula might bend during an unsuccessful attempt to enter a trocar or by excess force application during retinal penetration. Here we sought to validate whether modified cannulas can withstand similar mechanical stress. To simulate such scenarios, we mounted modified SI cannulas on a translation stage and moved them towards a rigid surface (i.e., aluminum mirror) using progressive perpendicular approaching. Upon contact with the rigid surface, the flexible tube started bending. We stopped the approaching once we visually assessed a 45 degrees angle between the polyimide tube and the rigid surface. Since the polyimide tube is semitransparent, we were able to use microscopy to measure the positioning of the probe in respect to its distal end (i.e., positioning offset). We did not observe damage to the encased fiber probes, but a small positioning offset in respect to the cannula tip. Figure 4(a) shows the positioning offset results for six bending tests performed with the same modified cannula. We found that the positioning offset lies between +17 and −11 µm. We further tested whether the mechanical stress would compromise the sensitivity of the probes. Figure 4(b) shows A-scans of an aluminum mirror placed at a distance of 600 µm in respect to six mechanically stressed probes. We found that the peak variability is on the order of 2dB. By adjusting the probe-mirror distance at 600 µm we compensated for the positioning offset in those measurements (i.e., the peak position is the

Biomedical Optics EXPRESS

same for all SI cannulas in Fig. 4(b)). Yet, one may expect a small angle between the polyimide tube and encased probe, and a small change in that angle due to the applied stress. We did not compensate for this potential misalignment. Thus, most likely the exiting beam hit the mirror with slightly different angles after each bending test, resulting to some SNR variability. These results indicate that the modified 36 SI cannulas can withstand mechanical stress without significant loss in sensitivity and that the resulting positioning offset is small considering the retinal thickness.

3.3. Ex-vivo validation of modified 36G SI cannulas

To validate the modified 36G SI cannulas, we performed a series of tests in ex-vivo porcine eyes purchased from a local butcher shop. Preliminary testing was performed without removing the vitreous. In those experiments we observed poor reproductivity in penetrating the retina. We attributed that to the presence of the hyaloid collagen membrane. Thus, we performed manual open sky removal of the vitreous for all eyes used in our core study. We used intraocular irrigating solution to fill the eye cavity. We then introduced the modified 36G SI cannulas into the eyeball, using the approach described in section 2.4. Figure 5 shows typical A-scan and M-scan signals acquired from ex-vivo porcine eyes, where the front and back parts of the retina can be clearly identified. In Fig. 5, the retina appears thicker than average pig retina (367 vs 290 μm [21]) because the approach angle of the SI cannula is not perpendicular to the retina. One can derive a 38° angle between the SI cannula and the retina considering the apparent retinal thickness.

Once the approach to the retina was completed, operators "clicked" the RPE layer, visually identified at the M-scan, to initiate the injection. We performed a total of 48 controlled injections in 39 eyes, including 8 test injections and 40 validation injections. We aimed for a 5 μL PBS injection by selecting 5 psi and 7.5 seconds for the injection pressure and duration, respectively. We used external OCT to rank each validation injection. If a retinal bleb was identified the injection was ranked as successful. Figure 6 shows an overview of the injection process visualized using external OCT, including the positioning of the modified SI cannula inside the retina after that automatic penetration (Fig. 6(a)), and the formation of a retinal bleb after the injection (Fig. 6(b)). A representative video of an OCT-controlled injection can be found in the Supplement 1 (see Visualization 1). Using external OCT for validation, we found that out of the 40 SI trials, 38 were successful, whereas 2 trials were unsuccessful, corresponding to a success rate of 95.0% (95% CI: 83.1–99.4).

3.4. Correlation between the subretinal bleb volume and injection volume for ex-vivo injections performed by modified 36G SI cannulas

To further validate the accuracy of the automatic injection system, we sought to determine what fraction of the injected liquid volume ended up in the subretinal space. To do so, we quantified the subretinal bleb volume using the method described in section 2.5. Briefly, we compared volumetric OCT scans before and after the SI (Fig. 7) and traced the displacement of the retinal front to calculate the subretinal bleb volume. To test whether this approach is sensitive to the SI process itself (i.e., retinal deformation), we inserted modified cannulas into the retina and retracted them without injecting. For three repetitions, the measured bleb volume was 0.03, 0.05 and -0.006 μL, i.e., at least 2-orders of magnitude smaller compared to the injection volume that we used in our study.

We performed 10 injections of 1 μL of saline in ex-vivo porcine eyes for quantifying potential liquid reflux. We used a smaller volume compared to the initial validation test to ensure that entire bleb was contained into a volumetric OCT scan. We found a mean bleb volume of 0.75 ± 0.23 μL, which indicates that 75% of the injected volume ends up at the subretinal space. The outcome for the individual SI is summarized in Table 1.

Biomedical Optics EXPRESS

Table 1. The calculated subretinal bleb volume for ten SI of 1 µL

SI (#)	1	2	3	4	5	6	7	8	9	10
Subretinal bleb volume (µL)	0.49	0.71	0.94	0.88	0.22	0.9	0.76	0.77	0.96	0.82

3.5. Proof-of-concept ex-vivo validation of modified commercial 40G SI cannulas

We validated further the feasibility of OCT-controlled injections using a modified commercial 40G SI metallic cannula. For those proof-of-concept experiments, we used freshly enucleated porcine eyes. Furthermore, a surgeon performed a pars plana vitrectomy before performing SI, as in clinical practice. SI were performed under an ophthalmic microscope; however, the latter was used only to validate their outcome. The surgeon injected 5 µL of indocyanine green (to facilitate visualization), using the approach described in section 3.3.

Figure 8 present the outcome of two representative injections. In the first injection (Fig. 8(a)), the injection depth was selected 75 µm above the RPE. Although we clearly identified the green dye under the retina, a reflux occurred at the injection site (area indicated with a dashed line in Fig. 8(a)). Liquid reflux is undesirable but not uncommon in SI injections [22]. In the second injection, we targeted penetration up to the RPE, and the injection was completed without reflux. The retinal detachment, which is the visual clue of a successful SI injection is hardly visible on those pictures, but it can be better appreciated in the videos provided in the Supplement 1 (see Visualization 2, Visualization 3). The videos present the microscope view as well as the front panel of the control program with the live feed of the OCT signal. Note that imaging with external OCT was not possible for those eyes because the focusing optics of the available OCT systems was not suitable for entire porcine eyes. Overall, proof-of-concept injections with modified commercial 40G SI cannulas showed reliable integration of the miniaturized probes and successfully completed controlled injections.

4. Discussion

For our core study we used home-made 36G flexible SI cannulas that are similar to those commonly used in the clinic, i.e., flexible 38G. In commercial 38G flexible SI cannulas, the back end of the polyimide tube is not accessible, thus it is impossible to insert the probe. To resolve this, we opted to fabricate our own 36G SI cannulas. Note that we did not fabricate 38G SI cannulas because we did not have access to commercially available 38G polyimide tubes. We showed that modified 36G polyimide SI cannulas have reproducible flow capacity, whereas the encased probes maintain their optical properties. The modified cannulas can withstand the typical stress encountered in a SI. However, they have compromised flow capacity (i.e., equivalent to commercial 48G SI cannulas), but this can be compensated by appropriate adjustment of the injection time. The injected drug volume in SI ranges from 100 [4] to 300 µL [25] and the typical injection time is 20 seconds for a 38G SI cannula. In those SI cannulas, 38G refers to the external diameter, whereas the inner diameter is 41G. Considering the reduced flow rate at given injection pressure due to the encased probe [Eq. (1)], one can estimate that ~ 60 seconds will be required to perform a SI using a modified 36G SI cannula. This limitation is not present in a similar approach that uses an OCT probe attached externally to 34G SI cannulas [18]. Yet this approach results in a much thicker assembly, which is a major limitation toward clinical adoption. This could be potentially mitigated by implementing probe miniaturization approaches implemented by us [20] and others [23].

Ex-vivo validation showed high SI success ratio (95%) and that the injected volume corresponds to 75% of the targeted volume. It was not possible to apply automatic RPE segmentation in detached retinas because we used an external OCT system that is not optimized for eye imaging. Therefore, we used an indirect method to measure the retinal bleb volume, i.e., monitoring of

Biomedical Optics EXPRESS

the displacement of the retinal front layer. Optimally, on may trace the RPE layer [24] to attain better accuracy in calculating the bleb volume. Note that we manually applied this quantification approach to a subset of our datasets for which manual segmentation of the RPE was feasible and found that our automatic approach overestimates the volume by ∼15%.

The semi-automated SI approach permits seamless injection at different injection angles without a need for angle-specific calibration. This is attained because the manipulator uses a fourth axis to move the SI cannula coaxial to the selected angle. In this work we used injection angles ranging from 35 to 55 degrees. Future studies can address if the injection angle and/or injection site affect the SI efficacy. There is virtually no limitation in performing multiple SI if the loaded drug is not generating strong OCT signal (i.e., comparable to that of the retina). In our experiments, we did perform up to 5 SI per eye using the same SI cannula without noticing any reproducibility problems. This number was limited by the volume of the preloaded model drug.

We estimate the cost of the materials (i.e., fibers and connectors) for transforming a 36G SI cannula to an OCT guided SI cannula to ∼ 25 USD. The components of the home-made OCT unit cost 7,800 USD. Considerable cost reduction, up to 3,500 USD, is feasible by cost-effective re-engineering of the system to downgrade components without comprising the overall performance. Altogether, these factors can favor translation of this technology to the clinic. Note that high-end iOCT cost few hundred thousand dollars. Those systems are designed to provide complementary imaging via integration with surgical microscopes [26–30] and not to execute precise SI. Moreover, in iOCT the SI cannula can obstruct the laser path and thus compromise retinal imaging at the injection site.

The developed system can have a direct impact in preclinical testing of therapies for retinal diseases as it offers a reproducible approach to deliver novel gene and cell therapies. Integration with a micromanipulator that uses a remote center of motion system would greatly improve the cannula placement inside the eye before injection. Further improvement of the guiding software can be attained by automatic real-time tracing of the retinal boundaries [31] using an M-scan. Clinical translation will require integration of this technology with platforms cleared for robotic-assisted eye surgery. Such robotic systems are already used in eye surgery applications, including remote SI [9]. Potential translation could be of particular benefit for patients suffering from late-stage RP and other degenerative diseases because they have a limited number of retinal cells that can be potentially targeted and rescued. Dose uncertainty elimination could also help to better understand why patients respond differently to the same treatment. Note that when performing SI surgeons may induce a pre-bleb with a saline solution to facilitate better access to the subretinal space. Our system could help avoid this step as it provides precise control over the injection depth. This may reduce the stress to the retinal tissue which has been reported to cause photoreceptor cell death [4].

5. Conclusion

In conclusion, we presented an approach to perform automated SI using clinically relevant 36 SI cannulas and commercial 40G SI cannulas. OCT probe miniaturization down to 70 µm has been central in our approach. Encased into the SI cannulas, the OCT probes generated M-scans of the retina that allowed users to select the injection depth using a simple intuitive interface. Modified SI cannulas were proved mechanically robust and efficient in delivering a model drug into ex-vivo porcine eyes. Potential clinical adoption of OCT-controlled SI systems can optimize the delivery of gene and cell therapies for retinal diseases. Naturally, this will require integration of this technology with platforms cleared for robotic-assisted eye surgery.

Funding. Vision Health Research Network (Quebec); Fonds de recherche en ophtalmologie de l'Université de Montréal; Fonds de Recherche du Québec - Santé (253123, 265459).

Acknowledgments. We thank Dr F. Rezende for providing us the vitrectomy machine used in this study and M. Marcoux (CRCHUM animal facility) for kindly providing us porcine eyes.

Biomedical Optics EXPRESS

Disclosures. The authors have no conflicts of interest to report.

Data availability. Data underlying the results presented in this paper are not publicly available at this time but may be obtained from the authors upon reasonable request.

Supplemental document. See Supplement 1 for supporting content.

References

1. Y. Peng, L. Tang, and Y. Zhou, "Subretinal injection: a review on the novel route of therapeutic delivery for vitreoretinal diseases," Ophthalmic Res. **58**(4), 217–226 (2017).
2. G. A. Ochakovski, K. Ulrich Bartz-Schmidt, and M. D. Fischer, "Retinal gene therapy: surgical vector delivery in the translation to clinical trials," Front. Neurosci. **11**(APR), 1–7 (2017).
3. K. Xue, T. L. Edwards, H. C. M. Meenink, M. J. Beelen, G. J. L. Naus, M. P. Simunovic, M. D. de Smet, and R. E. MacLaren, "Robot-assisted retinal surgery: overcoming human limitations," in M. Ohji, ed., *Retina Atlas* (Springer Singapore, 2019), pp. 109–114.
4. K. Xue, M. Groppe, A. P. Salvetti, and R. E. MacLaren, "Technique of retinal gene therapy: delivery of viral vector into the subretinal space," Eye **31**(9), 1308–1316 (2017).
5. V. Dave, P. Susaimanickam, I. Mir, I. Mariappan, S. Basu, B. Reddy, R. Pappuru, S. Jalali, and T. Das, "Learning curve of a trained vitreo-retinal surgeon in sub-retinal injections in a rat model: Implications for future clinical trials," Indian J. Ophthalmol. **67**(9), 1455–1458 (2019).
6. R. R. Hartman and U. B. Kompella, "Intravitreal, subretinal, and suprachoroidal injections: evolution of microneedles for drug delivery," J. Ocul. Pharmacol. Ther. **34**(1-2), 141–153 (2018).
7. R. Ladha, T. Meenink, J. Smit, and M. D. de Smet, "Advantages of robotic assistance over a manual approach in simulated subretinal injections and its relevance for gene therapy," Gene Ther. (2021).
8. J. Smits, A. Gijbels, K. Willekens, B. Stanzel, and D. Reynaerts, "Robot-assisted subretinal surgery: initial in-vivo animal validation," in *The Hamlyn Symposium on Medical Robotics* (The Hamlyn Centre, Faculty of Engineering, Imperial College London, 2019), pp. 91–92.
9. T. L. Edwards, K. Xue, H. C. M. Meenink, M. J. Beelen, G. J. L. Naus, M. P. Simunovic, M. Latasiewicz, A. D. Farmery, M. D. de Smet, and R. E. MacLaren, "First-in-human study of the safety and viability of intraocular robotic surgery," Nat. Biomed. Eng. **2**(9), 649–656 (2018).
10. S. Mukherjee, S. Yang, R. A. Maclachlan, L. A. Lobes, J. N. Martel, and C. N. Riviere, "Toward monocular camera-guided retinal vein cannulation with an actively stabilized handheld robot," *Proc. - IEEE Int. Conf. Robot. Autom.* 2951–2956 (2017).
11. S. L. Charreyron, Q. Boehler, A. N. Danun, A. Mesot, M. Becker, and B. J. Nelson, "A magnetically navigated microcannula for subretinal injections," IEEE Trans. Biomed. Eng. **68**(1), 119–129 (2021).
12. D. Huang, E. Swanson, C. Lin, J. Schuman, W. Stinson, W. Chang, M. Hee, T. Flotte, K. Gregory, C. Puliafito, and A. Et, "Optical coherence tomography," Science **254**(5035), 1178–1181 (1991).
13. J. G. Fujimoto, "Optical coherence tomography for ultrahigh resolution in vivo imaging," Nat. Biotechnol. **21**(11), 1361–1367 (2003).
14. O. M. Carrasco-Zevallos, C. Viehland, B. Keller, M. Draelos, A. N. Kuo, C. A. Toth, and J. A. Izatt, "Review of intraoperative optical coherence tomography: technology and applications [Invited]," Biomed. Opt. Express **8**(3), 1607 (2017).
15. R. Tadayoni, "Intraoperative OCT: Would You Like Some Extra Information?" Ophthalmol. Retin. **2**(4), 261–262 (2018).
16. S. Han, M. V. Sarunic, J. Wu, M. Humayun, and C. Yang, "Handheld forward-imaging needle endoscope for ophthalmic optical coherence tomography inspection," J. Biomed. Opt. **13**(2), 020505 (2008).
17. K. M. Joos and J.-H. Shen, "Miniature real-time intraoperative forward-imaging optical coherence tomography probe," Biomed. Opt. Express **4**(8), 1342 (2013).
18. J. Kang and G. Cheon, "Demonstration of subretinal injection using common-path swept source OCT guided microinjector," Appl. Sci. **8**(8), 1287 (2018).
19. J. Im and C. Song, "Oblique injection depth correction by a two parallel OCT sensor guided handheld SMART injector," Biomed. Opt. Express **12**(2), 926 (2021).
20. A. Abid, S. Mittal, and C. Boutopoulos, "Etching-enabled extreme miniaturization of graded-index fiber-based optical coherence tomography probes," J. Biomed. Opt. **25**(03), 1 (2019).
21. W. Xie, M. Zhao, S. H. Tsai, W. L. Burkes, L. B. Potts, W. Xu, H. R. Payne, T. W. Hein, L. Kuo, and R. H. Rosa, "Correlation of spectral domain optical coherence tomography with histology and electron microscopy in the porcine retina," Exp. Eye Res. **177**(4), 181–190 (2018).
22. P. D. Westenskow, T. Kurihara, S. Bravo, D. Feitelberg, Z. A. Sedillo, E. Aguilar, and M. Friedlander, "Performing subretinal injections in rodents to deliver retinal pigment epithelium cells in suspension," J. Vis. Exp. **95**(95), e52247 (2015).
23. M. Marrese, H. Offerhaus, E. Paardekam, and D. Iannuzzi, "70 Mm diameter optical probe for common-path optical coherence tomography in air and liquids," Opt. Lett. **43**(24), 5929 (2018).

Biomedical Optics EXPRESS

24. S. T. Hsu, H. Gabr, C. Viehland, K. Sleiman, H. T. Ngo, O. M. Carrasco-Zevallos, L. Vajzovic, R. P. McNabb, S. S. Stinnett, J. A. Izatt, A. N. Kuo, and C. A. Toth, "Volumetric measurement of subretinal blebs using microscope-integrated optical coherence tomography," Transl. Vis. Sci. Technol. **7**(2), 19 (2018).
25. S. Russell, J. Bennett, J. A. Wellman, D. C. Chung, Z. F. Yu, A. Tillman, J. Wittes, J. Pappas, O. Elci, S. McCague, D. Cross, K. A. Marshall, J. Walshire, T. L. Kehoe, H. Reichert, M. Davis, L. Raffini, L. A. George, F. P. Hudson, L. Dingfield, X. Zhu, J. A. Haller, E. H. Sohn, V. B. Mahajan, W. Pfeifer, M. Weckmann, C. Johnson, D. Gewaily, A. Drack, E. Stone, K. Wachtel, F. Simonelli, B. P. Leroy, J. F. Wright, K. A. High, and A. M. Maguire, "Efficacy and safety of voretigene neparvovec (AAV2-hRPE65v2) in patients with RPE65-mediated inherited retinal dystrophy: a randomised, controlled, open-label, phase 3 trial," Lancet **390**(10097), 849–860 (2017).
26. M. Zhou, X. Hao, A. Eslami, K. A. I. Huang, C. Cai, C. P. Lohmann, N. Navab, A. Knoll, and M. A. L. I. Nasseri, "6DOF needle pose estimation for robot-assisted vitreoretinal surgery," IEEE Access **7**, 63113–63122 (2019).
27. Y. Li, W. Zhang, V. P. Nguyen, R. Rosen, X. Wang, X. Xia, and Y. M. Paulus, "Real-time OCT guidance and multimodal imaging monitoring of subretinal injection induced choroidal neovascularization in rabbit eyes," Exp. Eye Res. **186**(July), 107714 (2019).
28. M. Sommersperger, J. Weiss, M. Ali Nasseri, P. Gehlbach, I. Iordachita, and N. Navab, "Real-time tool to layer distance estimation for robotic subretinal injection using intraoperative 4D OCT," Biomed. Opt. Express **12**(2), 1085 (2021).
29. M. Zhou, K. Huang, A. Eslami, H. Roodaki, D. Zapp, M. Maier, C. P. Lohmann, A. Knoll, and M. A. Nasseri, "Precision Needle Tip Localization Using Optical Coherence Tomography Images for Subretinal Injection," in *Proceedings - IEEE International Conference on Robotics and Automation* (2018).
30. M. Zhou, X. Wang, J. Weiss, A. Eslami, M. Maier, C. P. Lohmann, N. Navab, A. Knoll, and M. A. Nasseri, "Needle localization for robot-assisted subretinal injection based on deep learning," *IEEE Int. Conf. Robot. Autom.* 8727–8732 (2019).
31. S. Lee and J. U. Kang, "CNN-based CP-OCT sensor integrated with a subretinal injector for retinal boundary tracking and injection guidance," J. Biomed. Opt. **26**(06), 1–14 (2021).